Improved Analytic Model for Eddy Current Force Considering Edge-Effect of a Conductive Plate

S. Paul, J. Z. Bird

***Abstract* -- The eddy current induction in a conductive medium with finite width and thickness due to a moving magnetic rotor is studied. The presented formulation is based on the second order vector potential and the magnetic scalar potential and takes into account the magnetic field interaction through the edges of the conductive medium. The eddy current fields as well as thrust, lift and lateral force created by the rotational motion of the magnetic rotor have been computed and the accuracy and computation time have been compared with steady-state and transient finite element analysis results.**

***Index Terms*-- eddy current, edge-effect, Halbach, Maglev**

I. Introduction

RESEARCH has been conducted in the past to find integrated propulsion and suspension solutions with a passive guideway for magnetic levitated vehicles (maglev). The linear inductor motor (LIM) [1], self-excited linear synchronous motor [2] and electromagnetic river [3] are some of the ideas that have been proposed. In [4, 5] Fujii *et al.* proposed the use of magnetic rotors rotating above a conductive plate as a means of creating both propulsion and levitation force. More recently, Bird [6] proposed using an Electrodynamic Wheel (EDW) concept, as shown in Fig. 1, in which Halbach magnet rotors rotate and translationally move above a non-magnetic conductive plate. The induced eddy currents in the plate interact with the magnetic field of the Halbach rotor and lift the vehicle. The induced eddy currents also simultaneously create propulsion or drag force depending on the slip speed, s_l. The slip speed is defined as $s_l = \omega_m r_o - v_x$, where ω_m, v_x and r_o are the mechanical rotational speed [rads^{-1}], translational speed [ms^{-1}] and outer radius of the rotor [m]. If the slip speed is positive, propulsion force results and pushes the vehicle forward. But if it is negative, drag force is generated and slows the vehicle down. A 3D schematic of a single Halbach rotor above an aluminum plate is shown in Fig. 2 and schematic of such vehicle is shown in Fig. 3. A prototype model is shown in Fig. 4. In addition to lift and drag/thrust force there is a lateral force that may decenter the vehicle. Thus an accurate and quick eddy current force modeling is imperative for the study of the dynamics of such vehicle. Although finite element models are capable of computing the forces, analytical models are more appealing because of their computational efficiency.

This material is based upon work supported by the National Science Foundation under Grant No. 0925941.

S. Paul is with Nexteer Automotive, Saginaw, MI 48601 USA (e-mail: subhra.paul@nexteer.com).

J. Z. Bird is with the Department of Electrical and Computer Engineering, Portland State University, Portland, OR 97201 USA (e-mail: bird@pdx.edu).

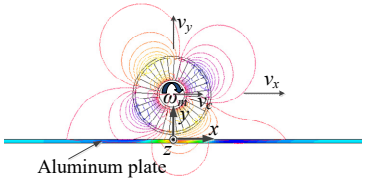

Fig. 1 A 2 pole-pair Halbach rotor rotating above an aluminum plate. Isoline plot of the radial flux density and isosurface plot of the eddy current density is shown

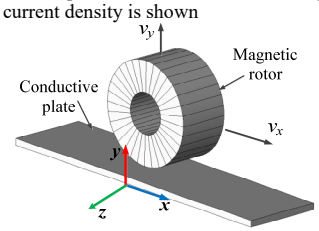

Fig. 2 A 3-D schematic of a single rotor above an aluminium plate.

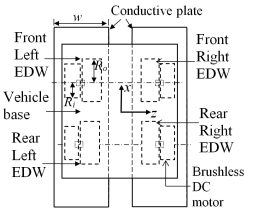

Fig. 3. The *x-z* view of a 2D schematic of the maglev vehicle

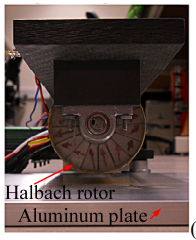

(a)

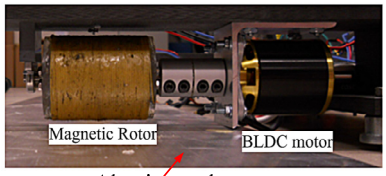

(b)

Fig. 4.View of one Halbach rotor on aluminium plate of experimental prototype vehicle

A plethora of research has been conducted to calculate eddy current fields in a conductive medium mostly in the context of eddy current testing and also for maglev vehicles. However, very few papers have considered the influence of the finite conductor plate width on the eddy current force. Urankar [7] presented a semi-analytic integral solution for the force acting on a conductive medium of arbitrary shape and finite width using the magnetic vector potential. However, in order to compute the force the integral equations need to be evaluated over the conductive domain as well as the exciter domain. The eddy current distribution due to the edge effect of a finite width conductive plate or conductive plate with a hole has been analytically derived using the second order vector potential [8, 9] and the magnetic vector potential [10]. Although these publications considered the finite width of the plate with hole or crack for impedance variation calculations, they did not consider the finite thickness of plate for force calculations [9-11]. Recently Pluk *et al.* [12] used a mirroring technique [13] to consider the finite length and width of a conductive plate and provided a semi-analytic solution for the induced current density. More recently Paul *et al.* [14] presented a simple, fast analytic model to compute the eddy current induced lift and thrust/drag force using only two components of the magnetic vector potential. However, the

accuracy of this analytic model degrades with increased plate thickness. To account for the edge effect, in [15] Paul *et. al.* modeled the side-air regions using the magnetic vector potential. This resulted in an improved thrust and lift force which is applicable to a plate of any thickness. However, the limitation of the models [14, 15] is explained in Fig. 5 [16] in which the flux density for a 15mm thick plate and 35mm lateral offset of the rotor is compared. It is observed that near the edge (i.e. z=0mm) the error in the analytically calculated B_y and B_z field increases which results in inaccurate lateral force calculation. The 2-component and 3-component analytic models refer to the models presented in [14] and [15] respectively.

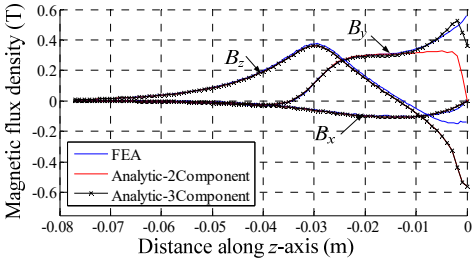

Fig. 5 Flux density comparison at x=0mm on the top plate surface. [16]

The contribution of this paper is to accurately model the edge effect in a conductive plate of finite thickness and width for the thrust, lift and lateral force computation. The results will be validated with finite element analysis (FEA). The assumptions of the proposed model are: (1) The plate length, l, is infinite but width, w, and thickness, h, are finite; (2) The plate is continuous, non-magnetic, linear and homogenous and (3) The magnetic source has only rotational motion.

II. Governing Equation Formulation

The x-y and y-z view of the problem domain are shown in Fig. 6. In order to achieve coupling between the fields in the plate, Ω_{II}, and side region, Ω_{IV}, in a mathematically elegant manner the fields in these regions can be modeled as Fourier series with eigenvalues determined by applying appropriate boundary conditions at the interface boundary, Γ_e.

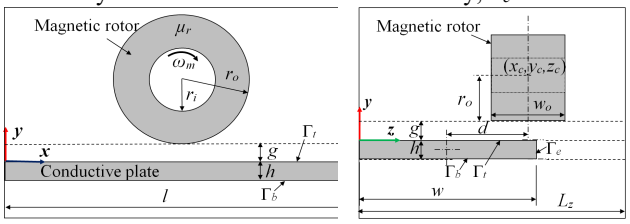

Fig. 6 (a) x-y and (b) y-z view of the problem domain showing lateral offset of magnetic rotor from the plate center.

The field of the magnetic rotor is required only in the boundary condition of boundary Γ_t in order to determine the eddy current fields. Hence, the simplified problem domain of Fig. 7 can be derived from Fig. 6 by omitting the rotor. In this paper the induced and reflected fields in the conductive region Ω_{II} and nonconductive region Ω_{IV} are modeled using second order vector potential (SOVP) [17] while the fields in the nonconductive regions Ω_I and Ω_{III} are modeled using magnetic scalar potential. Due to such a choice of potentials the number of unknowns in the problem domain has been kept to a minimum.

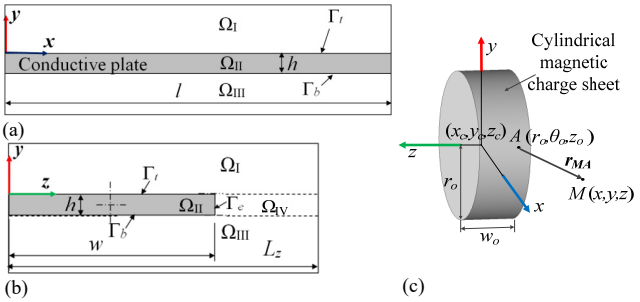

Fig. 7. (a) x-y and (b) y-z view of the reduced problem domain, (c) Halbach rotor enclosed in cylindrical charge sheet on its outer surface [18]

The solution domain (originally infinite) has been truncated along the x and z-directions with suitable boundary conditions while it is unconstrained along the y-axis. Thus the domain extends from 0 to l in the x-direction and from 0 to L_z in the z-direction. In this paper, perfect magnetic conduction (PMC) boundary condition has been applied at x=0 and perfect electric conduction condition (PEC) has been applied at x=l

$$B_i = 0, \quad i = y,z \text{ , at } x\text{=}0 \tag{1}$$

$$B_x = 0 \text{ , at } x\text{=}l \tag{2}$$

Along the z-axis, a PMC condition is applied at $z = 0, L_z$

$$B_i = 0, \quad i = x,y \text{ , at } z = 0, L_z \tag{3}$$

This choice of boundary conditions yields Fourier series with respect to x and z axes without zero frequency terms which greatly simplifies the solution procedure.

A. Conductive Region (Ω_{II})

Magnetic vector potential, **A**, and flux density, **B**, are related to the SOVP, **W**, as follows [17]

$$\mathbf{A} = \nabla \times \mathbf{W}, \ \mathbf{B} = \nabla \times \mathbf{A} \tag{4}$$

W can be split into transverse electric (TE), W_a, and transverse magnetic (TM), W_b, scalar potentials with z-preferred direction as follows

$$\mathbf{W} = \hat{z}W_a + \hat{z} \times \nabla W_b \tag{5}$$

Here $\hat{z}$ is the unit vector along the z-direction. A steady state solution for the scalar TE and TM potentials is assumed as

$$W_i(x,y,z,t) = W_i^k(x,y,z)e^{-j\omega_e t}, \quad i = a,b; k = II,IV \tag{6}$$

where ω_e is the electrical rotational speed of the rotor [rad/s]. The TE and TM potentials satisfy the following

$$\frac{\partial^2 W_i^{II}}{\partial x^2} + \frac{\partial^2 W_i^{II}}{\partial y^2} + \frac{\partial^2 W_i^{II}}{\partial z^2} = \varepsilon^2 W_i^{II}, \ i = a,b, \tag{7}$$

where $\varepsilon^2 = -j\mu_0\sigma\omega_e$, σ = plate conductivity[Sm^{-1}]. The normal component of the eddy current or the magnetic vector potential should be zero at the plate edges i.e. at z=0 and z=w

$$A_z = 0 \text{ , at } z\text{=}0, w \tag{8}$$

From (4) it can be noticed that with the z-preferred direction of the SOVP, given by (5), the A_z component is a function of the W_b potential only. Hence the boundary condition (8) can be satisfied by choosing suitable Fourier representation of only the W_b potential. Equation (7) can be solved using separation of variable method and boundary conditions (1)-(3), (8)

$$W_a^{II}(x,y,z) = \sum_{m=1}^{M}\sum_{n=1}^{N_z} \sin(\xi_m x)\cos(q_n z)(C_{mn}^a e^{\alpha_{mn} y} + D_{mn}^a e^{-\alpha_{mn} y}) \tag{9}$$

$$W_b^{\mathrm{II}}(x,y,z)=\sum_{m=1}^{M}\sum_{n=1}^{N_r}\cos(\xi_m x)\sin(r_n z)(C_{mn}^{b}e^{\beta_{mn}y}+D_{mn}^{b}e^{-\beta_{mn}y}) \quad (10)$$

where
$$\xi_m=\frac{\pi(2m-1)}{2l},\ 1\le m\le\infty \quad (11)$$

$$r_n=n\pi\ /\ w,\ 1\le n\le\infty \quad (12)$$

$$\alpha_{mn}=\sqrt{\xi_m^2+q_n^2+\varepsilon^2} \quad (13)$$

$$\beta_{mn}=\sqrt{\xi_m^2+r_n^2+\varepsilon^2} \quad (14)$$

The eigenvalues q_n are determined from the continuity condition of the magnetic flux density and field intensity at z=w and will be discussed in section III.A. It must also be noted that (9) and (10) have different numbers of harmonics along the z-axis. The logic behind this will also be discussed in section III.A.

B. Nonconductive Region Ω_{IV}

The TM potential does not contribute to the magnetic field in Ω_{IV} and hence is not modeled. The TE potential satisfies

$$\frac{\partial^2 W_a^{\mathrm{IV}}}{\partial x^2}+\frac{\partial^2 W_a^{\mathrm{IV}}}{\partial y^2}+\frac{\partial^2 W_a^{\mathrm{IV}}}{\partial z^2}=0\,,\ \text{in}\ \Omega_{\mathrm{IV}} \quad (15)$$

The following general solution for the TE potential can be obtained which satisfies (1)-(3)

$$W_a^{\mathrm{IV}}(x,y,z)=\sum_{m=1}^{M}\sum_{n=1}^{N_z}\sin(\xi_m x)\cos(p_n(L_z\text{-}z))(C_{mn}^{\mathrm{IV}}e^{\varpi_{mn}y}+D_{mn}^{\mathrm{IV}}e^{-\varpi_{mn}y}) \quad (16)$$

where
$$\varpi_{mn}=\sqrt{\xi_m^2+p_n^2} \quad (17)$$

and eigenvalues p_n need to be determined from the boundary condition at z=w as described in section III.A. However, to match region Ω_{II} with region Ω_{IV} on a term-by-term basis, their y-dependency can be chosen to be equal i.e

$$\varpi_{mn}=\alpha_{mn} \quad (18)$$

This implies,
$$p_n^2=q_n^2+\varepsilon^2 \quad (19)$$

Also the TE potential coefficients in Ω_{IV} can be expressed as a linear function of the coefficients in Ω_{II}

$$C_{mn}^{\mathrm{IV}}=a_{mn}C_{mn}^{a};\quad D_{mn}^{\mathrm{IV}}=a_{mn}D_{mn}^{a} \quad (20)$$

where a_{mn} is a linear factor and will be determined in section III.A. Using (18)-(20), (16) becomes

$$W_a^{\mathrm{IV}}=\sum_{m=1}^{M}\sum_{n=1}^{N_z}\sin(\xi_m x)\cos(p_n(L_z\text{-}z))a_{mn}(C_{mn}^{a}e^{\alpha_{mn}y}+D_{mn}^{a}e^{-\alpha_{mn}y}) \quad (21)$$

C. Nonconductive Regions Ω_I and Ω_{III}

The fields in Ω_{I}, Ω_{III} are modeled using the magnetic scalar potential, φ. In the absence of free current the magnetic scalar potential satisfies the following Laplace equation

$$\mu_0\nabla^2\phi=0\,,\quad \text{in}\ \Omega_{\mathrm{I}},\Omega_{\mathrm{III}} \quad (22)$$

Using the separation of variable method and applying boundary conditions (1)-(3), (22) can be solved to yield the fields as

$$\phi^{\mathrm{I}}(x,y,z)=\sum_{m=1}^{M}\sum_{n=1}^{N_z}A_{mn}^{\mathrm{I}}\sin(\xi_m x)\sin(k_n z)e^{-\kappa_{mn}y} \quad (23)$$

$$\phi^{\mathrm{III}}(x,y,z)=\sum_{m=1}^{M}\sum_{n=1}^{N_z}A_{mn}^{\mathrm{III}}\sin(\xi_m x)\sin(k_n z)e^{\kappa_{mn}(y+h)} \quad (24)$$

where
$$k_n=n\pi\ /\ L_z \quad (25)$$

$$\kappa_{mn}=\sqrt{k_n^2+\xi_m^2} \quad (26)$$

The y-dependency of (23)-(24) is chosen to decay the reflected and transmitted fields in regions Ω_{I}, Ω_{III} away from the conductive plate.

D. Source field modeling

The magnetic field of a Halbach rotor has been analytically modeled in 2D in [19]. In order to compute the fields in 3D the rotor is assumed to be wrapped in a cylindrical charge sheet [18], as shown in Fig. 7(c), and the charge density is assumed to be uniform along the z-axis as the magnetization is uniform along this direction. The charge density is related to the Halbach rotor radial flux density at the charge sheet location by [18]

$$\rho_{ms}(r_o,\theta_o)=2B_r^s(r_o)e^{jP\theta_o}[u(z+w_o\ /\ 2)-u(z-w_o\ /\ 2)] \quad (27)$$

where, w_o is the Halbach rotor width. The radial flux density at radial distance r from the center of the rotor can be computed from [19]

$$B_r^s(r)=\frac{2B_{rem}P(1+\mu_r)(r_i^{P+1}-r_o^{P+1})r_o^{2P}}{(1+P)[(1-\mu_r)^2r_i^{2P}-(1+\mu_r)^2r_o^{2P}]}\frac{1}{r^{P+1}} \quad (28)$$

where, μ_r, P, r_o, r_i and B_{rem} are the relative permeability, number of pole-pair, outer radius, inner radius and remanent flux density of the rotor respectively. With the knowledge of charge density the magnetic scalar potential at any point, M (x,y,z), in space external to the rotor can be calculated [18]

$$\phi^s(x,y,z)=\frac{B_r^s(r_o)}{2\pi\mu_0}\int_0^{2\pi}\int_{-w_o/2}^{w_o/2}\frac{e^{jP\theta_o}}{r_{MA}}dz_o d\theta_o \quad (29)$$

where, $\mathbf{r}_{MA}$=$(x\text{-}x_c\text{-}r_o\cos\theta_o)\hat{x}+(y\text{-}y_c\text{-}r_o\sin\theta_o)\hat{y}+(z\text{-}z_c\text{-}z_o)\hat{z}$ (30)

For generality, the origin of the Halbach rotor is located at (x_c,y_c,z_c). In (29) the integration with respect to z_o is performed analytically whereas integration with respect to θ_o is accomplished numerically. However, the source field needs to be represented with a Fourier series with the same eigenvalues as the scalar potential in regions Ω_{I}, Ω_{III}. A 2D discrete Fourier Transform is applied on the scalar field computed using (29) on the top plate surface, Γ_t i.e. at y=0 to represent the field as

$$\phi^s(x,0,z)=\sum_{m=1}^{M}\sum_{n=1}^{N_z}S_{mn}^{\phi}\sin(\xi_m x)\sin(k_n z)\,,\ \text{on}\ \Gamma_t \quad (31)$$

where, ξ_m and k_n are defined in (11) and (25), respectively.

III. Field Solution

A. Determination of unknown eigenvalues

In order to determine the unknown eigenvalues p_n and q_n, the continuity condition of the magnetic flux density and field intensity is applied at z=w. From the continuity of the normal component of the flux density, B_z, one obtains

$$\cos(q_n w)=\cos\big(p_n(L_z-w)\big)a_{mn} \quad (32)$$

From the continuity of the tangential component (B_x and B_y) of the flux density (noting unity relative permeability

throughout in the problem domain)

$$-\sin(q_n w)q_n = \sin\big(p_n(L_z - w)\big)p_n a_{mn} \tag{33}$$

Dividing (33) by (32) gives

$$\tan(q_n w)q_n + \tan\big(p_n(L_z - w)\big)p_n = 0 \tag{34}$$

Using (19), (34) can be written as

$$\sqrt{p_n^2 - \varepsilon^2}\tan\Big(w\sqrt{p_n^2 - \varepsilon^2}\Big) + p_n \tan\big(p_n(L_z - w)\big) = 0 \tag{35}$$

Equation (35) is solved numerically using Newton-Raphson iteration scheme to find p_n. Equations (19) and (32) are then used to calculate q_n and a_{mn} respectively. For detailed discussion on the root finding algorithm the reader can refer to [8]. Another numerical aspect of this formulation is the choice of the maximum summation index N_z and N_r. The choice of N_z depends on the value of L_z. Generally the larger the problem domain, the greater is the number of required terms [10]. For the simulations presented in this paper N_z has been chosen to be 64 for L_z=200mm. It is observed that choosing $N_r \sim N_z$ may make the system of equations ill-conditioned. Hence choosing the ratio of $N_r/N_z \sim w/L_z$ keep the condition number sufficiently low [8].

B. Determination of unknown coefficients

In order to determine the unknown Fourier series coefficients of the fields, the boundary condition is applied at y=0 and -h. From the continuity of B_x at y=0 for each m

$$-\mu_0\sum_{n=1}^{N_z}\sin(k_n z)\xi_m\Big(S_{mn}^{\phi} + A_{mn}^{\mathrm{I}}\Big) = \begin{cases} -\sum_{n=1}^{N_z}\sin(q_n z)\xi_m q_n\Big(C_{mn}^{a} + D_{mn}^{a}\Big) \\ \quad +\varepsilon^2\sum_{n=1}^{N_r}\sin(r_n z)\beta_{mn}\Big(C_{mn}^{b} - D_{mn}^{b}\Big), 0 < z < w \\ \sum_{n=1}^{N_z}\sin\big(p_n(L_z - z)\big)\xi_m p_n a_{mn}\Big(C_{mn}^{a} + D_{mn}^{a}\Big),\ w < z < L_z \end{cases} \tag{36}$$

Multiplying both sides by sin($k_i z$) and integrating from z=0 to L_z gives

$$-\mu_0 0.5L_z\xi_m(\bar{\mathbf{S}}_m^{\phi} + \bar{\mathbf{A}}_m^{\mathrm{I}}) = \xi_m\mathbf{M}^{(1)}(\bar{\mathbf{C}}_m^{a} + \bar{\mathbf{D}}_m^{a}) + \varepsilon^2\mathbf{M}^{(2)}\mathbf{b}_m(\bar{\mathbf{C}}_m^{b} - \bar{\mathbf{D}}_m^{b}) \tag{37}$$

where,

$$\mathbf{M}^{(1)} = -q_n\int_0^{w}\sin(k_i z)\sin(q_n z)dz + p_n a_{mn}\int_w^{L_z}\sin(k_i z)\sin[p_n(L_z - z)]dz,\ [N_z \times N_z] \tag{38}$$

$$\mathbf{M}^{(2)} = \int_0^{w}\sin(k_i z)\sin(r_n z)dz,\quad [N_z \times N_r] \tag{39}$$

$$\mathbf{b}_m = \mathrm{diag}[\beta_{mn}],\quad [N_r \times N_r] \tag{40}$$

$\bar{\mathbf{S}}_m^{\phi}$, $\bar{\mathbf{A}}_m^{\mathrm{I}}$, $\bar{\mathbf{C}}_m^{a}$, $\bar{\mathbf{D}}_m^{a}$ are vectors quantities of dimension $[N_z \times 1]$ whereas $\bar{\mathbf{C}}_m^{b}$, $\bar{\mathbf{D}}_m^{b}$ are vectors of dimension $[N_r \times 1]$. From the continuity of B_y at y=0, for each m

$$-\mu_0 0.5L_z\mathbf{k}_m(\bar{\mathbf{S}}_m^{\phi} - \bar{\mathbf{A}}_m^{\mathrm{I}}) = \mathbf{M}^{(1)}\mathbf{a}_m(\bar{\mathbf{C}}_m^{a} - \bar{\mathbf{D}}_m^{a}) + \varepsilon^2\xi_m\mathbf{M}^{(2)}(\bar{\mathbf{C}}_m^{b} + \bar{\mathbf{D}}_m^{b}) \tag{41}$$

where,

$$\mathbf{k}_m = \mathrm{diag}[\kappa_{mn}],\quad [N_z \times N_z] \tag{42}$$

$$\mathbf{a}_m = \mathrm{diag}[\alpha_{mn}],\quad [N_z \times N_z] \tag{43}$$

From the continuity of B_z at y=0, for each m

$$-\mu_0 0.5L_z\mathbf{K}\Big(\bar{\mathbf{S}}_m^{\phi} + \bar{\mathbf{A}}_m^{\mathrm{I}}\Big) = \mathbf{M}^{(3)}(\bar{\mathbf{C}}_m^{a} + \bar{\mathbf{D}}_m^{a}) \tag{44}$$

where,

$$\mathbf{K} = \mathrm{diag}[k_n],\quad [N_z \times N_z] \tag{45}$$

$$\mathbf{M}^{(3)} = -p_n^2\int_0^{w}\cos(k_i z)\cos(q_n z)dz - p_n^2 a_{mn}\int_w^{L_z}\cos(k_i z)\cos[p_n(L_z - z)]dz \tag{46}$$

Next, boundary conditions are applied at y= -h. Applying the continuity of the B_x at y= -h yields

$$-\mu_0 0.5L_z\xi_m\bar{\mathbf{A}}_m^{\mathrm{III}} = \xi_m\mathbf{M}^{(1)}(\bar{\mathbf{C}}_m^{a}\mathbf{e}^{-\mathbf{a}_m h} + \bar{\mathbf{D}}_m^{a}\mathbf{e}^{\mathbf{a}_m h}) + \varepsilon^2\mathbf{M}^{(2)}\mathbf{b}_m(\bar{\mathbf{C}}_m^{b}\mathbf{e}^{-\mathbf{b}_m h} - \bar{\mathbf{D}}_m^{b}\mathbf{e}^{\mathbf{b}_m h}) \tag{47}$$

where,

$$\mathbf{e}^{-\mathbf{a}_m h} = \mathrm{diag}[e^{-\alpha_{mn}h}],\quad [N_z \times N_z] \tag{48}$$

$$\mathbf{e}^{-\mathbf{b}_m h} = \mathrm{diag}[e^{-\beta_{mn}h}],\quad [N_r \times N_r] \tag{49}$$

From the continuity of B_y at y= -h the following is obtained

$$-\mu_0 0.5L_z\mathbf{k}_m\bar{\mathbf{A}}_m^{\mathrm{III}} = \mathbf{M}^{(1)}\mathbf{a}_m(\bar{\mathbf{C}}_m^{a}\mathbf{e}^{-\mathbf{a}_m h} - \bar{\mathbf{D}}_m^{a}\mathbf{e}^{\mathbf{a}_m h}) + \varepsilon^2\xi_m\mathbf{M}^{(2)}(\bar{\mathbf{C}}_m^{b}\mathbf{e}^{-\mathbf{b}_m h} + \bar{\mathbf{D}}_m^{b}\mathbf{e}^{\mathbf{b}_m h}) \tag{50}$$

From the continuity of B_z field at y=-h

$$-\mu_0 0.5L_z\mathbf{K}\bar{\mathbf{A}}_m^{\mathrm{III}} = \mathbf{M}^{(3)}(\bar{\mathbf{C}}_m^{a}\mathbf{e}^{-\mathbf{a}_m h} + \bar{\mathbf{D}}_m^{a}\mathbf{e}^{\mathbf{a}_m h}) \tag{51}$$

Equations (37), (41), (44), (47), (50), (51) can be written as

$$\mathbf{A}\bar{\mathbf{x}} = \bar{\mathbf{b}} \tag{52}$$

where,

$$\mathbf{A} = \begin{bmatrix} \mathbf{A}_1 & \mathbf{A}_1 & \mathbf{B}_1 & -\mathbf{B}_1 \\ \mathbf{A}_{2c} & \mathbf{A}_{2d} & \mathbf{B}_2 & \mathbf{B}_2 \\ \mathbf{A}_1\mathbf{e}^{-\mathbf{a}_m h} & \mathbf{A}_1\mathbf{e}^{\mathbf{a}_m h} & \mathbf{B}_1\mathbf{e}^{-\mathbf{b}_m h} & -\mathbf{B}_1\mathbf{e}^{\mathbf{b}_m h} \\ \mathbf{A}_{2d}\mathbf{e}^{-\mathbf{a}_m h} & \mathbf{A}_{2c}\mathbf{e}^{\mathbf{a}_m h} & -\mathbf{B}_2\mathbf{e}^{-\mathbf{b}_m h} & -\mathbf{B}_2\mathbf{e}^{\mathbf{b}_m h} \end{bmatrix} \tag{53}$$

$$\bar{\mathbf{x}} = \begin{bmatrix} \bar{\mathbf{C}}_m^{a} & \bar{\mathbf{D}}_m^{a} & \bar{\mathbf{C}}_m^{b} & \bar{\mathbf{D}}_m^{b} \end{bmatrix}^T \tag{54}$$

$$\bar{\mathbf{b}} = \begin{bmatrix} 0 & -\mu_0 L_z\mathbf{k}_m\bar{\mathbf{S}}_m^{\phi} & 0 & 0 \end{bmatrix}^T \tag{55}$$

$$\mathbf{A}_1 = \xi_m\Big[\mathbf{K}^{-1}\mathbf{M}^{(3)} - \mathbf{M}^{(1)}\Big];\mathbf{B}_1 = -\varepsilon^2\mathbf{M}^{(2)}\mathbf{b}_m;\mathbf{B}_2 = \varepsilon^2\xi_m\mathbf{M}^{(2)} \tag{56}$$

$$\mathbf{A}_{2c} = [\mathbf{k}_m\mathbf{K}^{-1}\mathbf{M}^{(3)} + \mathbf{M}^{(1)}\mathbf{a}_m];\mathbf{A}_{2d} = [\mathbf{k}_m\mathbf{K}^{-1}\mathbf{M}^{(3)} - \mathbf{M}^{(1)}\mathbf{a}_m] \tag{57}$$

Matrix A is of dimension $[4N_z \times 2(N_z + N_r)]$ whereas vectors $\bar{\mathbf{x}}$ and $\bar{\mathbf{b}}$ have the dimension of $[2(N_z + N_r) \times 1]$ and $[4N_z \times 1]$, respectively. Matrix $\mathbf{A}$ is asymmetric, but it has full column rank. Thus its left pseudo-inverse is a fairly accurate representation of its true inverse and $\bar{\mathbf{x}}$ can be obtained by solving (58), where $\mathbf{A}^{+}$ is the pseudo-inverse of $\mathbf{A}$ and is computed in Matlab.

$$\bar{\mathbf{x}} = \mathbf{A}^{+}\bar{\mathbf{b}} \tag{58}$$

IV. Force Calculation

Maxwell stress tensor using the magnetic flux induced in the conductive medium is used to calculate the forces. Thrust force is calculated using

$$F_x = \frac{1}{2\mu_0}\left[\int_0^{l}\int_0^{w}B_x^{\mathrm{II}}B_y^{\mathrm{II}*}\Big|_{y=0}dzdx - \int_0^{l}\int_0^{w}B_x^{\mathrm{II}}B_y^{\mathrm{II}*}\Big|_{y=-h}dzdx\right] + \frac{1}{2\mu_0}\int_0^{l}\int_{-h}^{0}B_x^{\mathrm{II}}B_z^{\mathrm{II}*}\Big|_{z=w}dydx \tag{59}$$

The first two integrals calculate force from top, Γ_t and bottom, Γ_b surfaces whereas the third one computes force from side surface, Γ_e. Lift force is calculated using

$$F_y = \frac{1}{4\mu_0}\int_0^l\int_0^w \left(B_y^{\text{II}}B_y^{\text{II}*} - B_x^{\text{II}}B_x^{\text{II}*} - B_z^{\text{II}}B_z^{\text{II}*}\right)\Big|_{y=0} dzdx$$
$$-\frac{1}{4\mu_0}\int_0^l\int_0^w \left(B_y^{\text{II}}B_y^{\text{II}*} - B_x^{\text{II}}B_x^{\text{II}*} - B_z^{\text{II}}B_z^{\text{II}*}\right)\Big|_{y=-h} dzdx$$
$$+\frac{1}{2\mu_0}\int_0^l\int_{-h}^0 B_y^{\text{II}}B_z^{\text{II}*}\Big|_{z=w} dydx \quad (60)$$

Lateral force is calculated using

$$F_z = \frac{1}{2\mu_0}\left[\int_0^l\int_0^w B_z^{\text{II}}B_y^{\text{II}*}\Big|_{y=0} dzdx - \int_0^l\int_0^w B_z^{\text{II}}B_y^{\text{II}*}\Big|_{y=-h} dzdx\right]$$
$$+\frac{1}{4\mu_0}\int_0^l\int_{-h}^0 (B_z^{\text{II}}B_z^{\text{II}*} - B_x^{\text{II}}B_x^{\text{II}*} - B_y^{\text{II}}B_y^{\text{II}*})\Big|_{z=w} dydx \quad (61)$$

Detailed expression for each component of the thrust, lift and lateral force is provided in the Appendix.

V. Model Validation

A. Field Validation

The geometric and material properties of the Halbach rotor and conductive plate are listed in Table 1. The induced magnetic flux density in the conductive plate has been compared against a previously developed 3-D FEA steady state model [6] for 25mm lateral offset of the rotor with flux density and field intensity continuity condition set at the interface of the conductive plate and surrounding air region in the FEA. Fig. 8 shows the flux density comparison on the top surface of the conductive plate across the *z*-axis. An excellent field match has been obtained.

Table 1 Simulation Parameters

	Description	Value	Unit
Halbach rotor	Outer radius, r_o	26	mm
	Inner radius, r_i	9.62	mm
	Width, w_o	52	mm
	Remanent flux density, B_{rem}	1.42	T
	Relative permeability, μ_r	1.108	-
	Pole pair number, P	2	-
Conductive plate	Conductivity, σ	2.459×10^7	Sm^{-1}
	Width, w	77	mm
	Length, l	200	mm
	Thickness, h	6.3	mm
	Air-gap between rotor and plate, g	9.5	mm

Table 2 Computation time for analytic and FEA models

Model type	Computation time
JMAG transient	5 hr 40 min
Current sheet based Comsol steady state model	8 min
Proposed analytic model using SOVP	32 s

B. Force Validation

The electromagnetic forces are compared with an FEA steady state model developed using Comsol and JMAG for different lateral offset and rotational speed values. The results are shown in Fig. 9-Fig. 10. A very good match of the forces has been achieved. The average computation time using a Dell E5520 workstation for a single rotational speed by the FEA and analytic models are listed in Table 2. The computation time of the proposed analytic model is longer than the model presented in [14]. This is mainly due to the need for the numerical computation of complex valued eigenvalues. Hence, if the eigenvalues can be calculated beforehand and stored in a look-up table, the analytic model can be made faster. The average accuracy of the developed analytic model with respect to JMAG and Comsol FEA models [6] has been compared as shown in Table 3

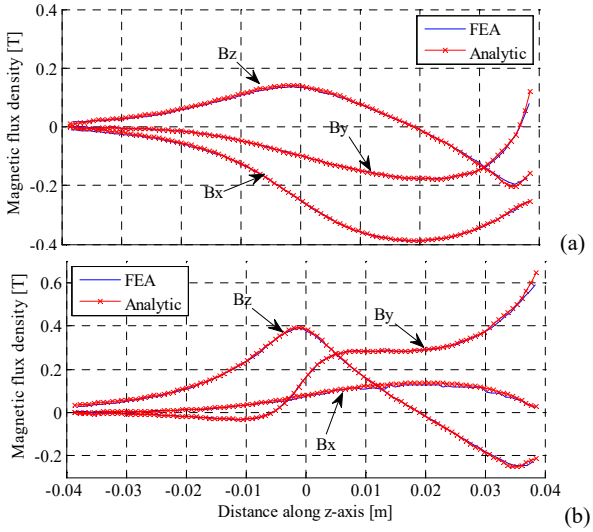

Fig. 8 Induced flux density comparison on the top surface of the conductive plate at (a) x=20mm and (b) x= 0mm for 25mm lateral offset of the rotor at zero translational velocity and 8000 RPM

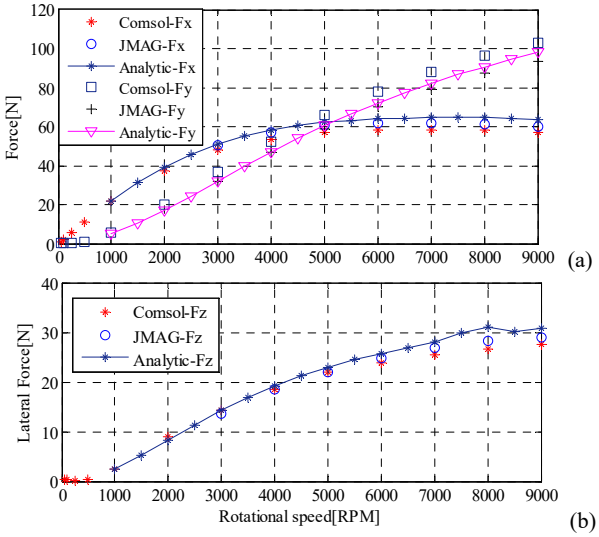

Fig. 9 Comparisons of (a) F_x, F_y and (b) F_z for 25mm lateral offset of the rotor at zero translational velocity.

Table 3 Accuracy of the developed analytic steady state model

Force	Avg. Error with JMAG [%]	Avg. Error with Comsol [%]
Thrust	4.32	7.95
Lift	3.04	5.8
Lateral	3.3	6.23

VI. Conclusion

An analytic 3-D steady state model of the eddy current distribution in a conductive plate has been developed considering the edge effect of the plate. The accuracy of the proposed model has been confirmed by comparison with FEA results. However, the accuracy comes at the cost of computational burden due to the numerical calculation of the

eigenvalues which can be improved with the use of a look up table.

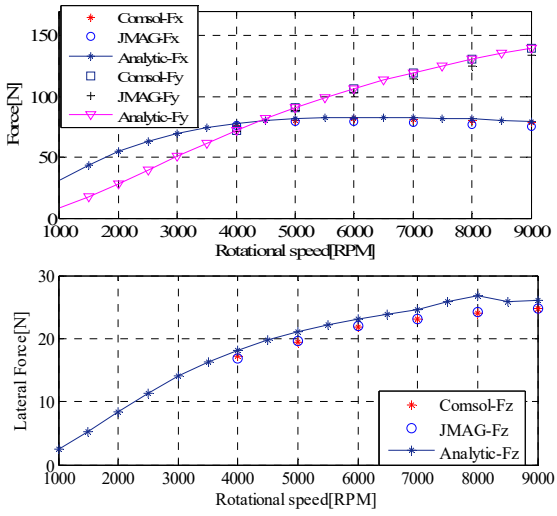

Fig. 10 Comparisons of (a) F_x, F_y and (b) F_z for 15mm lateral offset of the rotor at zero translational velocity.

VII. Appendix

A. Thrust force

The thrust force from the top plate surface is

$$F_x^{top}=\frac{1}{2\mu_0}\Bigg[\sum_{m=1}^{M}\sum_{n=1}^{N_z}\sum_{i=1}^{M}\sum_{l=1}^{N_z} I_{mi}^{x} I_{nl}^{z1}\xi_m q_n (C_{mn}^{a}+D_{mn}^{a}) q_l^{*}\alpha_{il}^{*}(C_{il}^{a*}-D_{il}^{a*}) - \varepsilon^{2*}\sum_{m=1}^{M}\sum_{n=1}^{N_z}\sum_{i=1}^{M}\sum_{l=1}^{N_r} I_{mi}^{x} I_{nl}^{z2}\xi_m q_n (C_{mn}^{a}+D_{mn}^{a})\xi_i (C_{il}^{b*}+D_{il}^{b*}) - \varepsilon^{2}\sum_{m=1}^{M}\sum_{n=1}^{N_r}\sum_{i=1}^{M}\sum_{l=1}^{N_z} I_{mi}^{x} I_{nl}^{z3}\beta_{mn} (C_{mn}^{b}-D_{mn}^{b}) q_l^{*}\alpha_{il}^{*}(C_{il}^{a*}-D_{il}^{a*}) + \varepsilon^{2}\varepsilon^{2*}\sum_{m=1}^{M}\sum_{n=1}^{N_r}\sum_{m=1}^{M}\sum_{n=1}^{N_r} I_{mi}^{x} I_{nl}^{z4}\beta_{mn} (C_{mn}^{b}-D_{mn}^{b})\xi_i (C_{il}^{b*}+D_{il}^{b*})\Bigg] \quad (62)$$

where * superscript indicates complex conjugation and

$$I_{mi}^{x}=\begin{cases}0.5\left[\dfrac{1-\cos\left[(\xi_i+\xi_m)l\right]}{(\xi_i+\xi_m)}+\dfrac{1-\cos\left[(\xi_i-\xi_m)l\right]}{(\xi_i-\xi_m)}\right], & \xi_i\neq\xi_m\\ 0.5\left[\dfrac{1-\cos\left[(\xi_i+\xi_m)l\right]}{(\xi_i+\xi_m)}\right], & \xi_i=\xi_m\end{cases} \quad (63)$$

$$I_{nl}^{z1}=0.5\left[\frac{\sin\left[(q_n-q_l^{*})w\right]}{(q_n-q_l^{*})}-\frac{\sin\left[(q_n+q_l^{*})w\right]}{(q_n+q_l^{*})}\right] \quad (64)$$

$$I_{nl}^{z2}=0.5\left[\frac{\sin\left[(q_n-r_l)w\right]}{(q_n-r_l)}-\frac{\sin\left[(q_n+r_l)w\right]}{(q_n+r_l)}\right] \quad (65)$$

$$I_{nl}^{z3}=0.5\left[\frac{\sin\left[(r_n-q_l^{*})w\right]}{(r_n-q_l^{*})}-\frac{\sin\left[(r_n+q_l^{*})w\right]}{(r_n+q_l^{*})}\right] \quad (66)$$

$$I_{nl}^{z4}=\begin{cases}0, & r_n\neq r_l\\ w/2, & r_n=r_l\end{cases} \quad (67)$$

The force from the bottom surface Γ_b can be computed from (62) by replacing C_{mn}^{a}, D_{mn}^{a}, C_{mn}^{b} and D_{mn}^{b} with $C_{mn}^{a}e^{-\alpha_{mn}h}$, $D_{mn}^{a}e^{\alpha_{mn}h}$, $C_{mn}^{b}e^{-\beta_{mn}h}$ and $D_{mn}^{b}e^{\beta_{mn}h}$ respectively. The following computes the thrust force from edge surface Γ_e

$$F_x^{side}=\frac{1}{2\mu_0}\sum_{m=1}^{M}\sum_{n=1}^{N_z}\sum_{i=1}^{M}\sum_{l=1}^{N_z} I_{mi}^{x}\sin(q_n w)\xi_m q_n\cos(q_l^{*}w)p_l^{2*}\left[C_{mn}^{a}C_{il}^{a*}\frac{1-e^{-(\alpha_{mn}+\alpha_{il}^{*})h}}{(\alpha_{mn}+\alpha_{il}^{*})}+C_{mn}^{a}D_{il}^{a*}\frac{1-e^{-(\alpha_{mn}-\alpha_{il}^{*})h}}{(\alpha_{mn}-\alpha_{il}^{*})} - D_{mn}^{a}C_{il}^{a*}\frac{1-e^{(\alpha_{mn}-\alpha_{il}^{*})h}}{(\alpha_{mn}-\alpha_{il}^{*})}-D_{mn}^{a}D_{il}^{a*}\frac{1-e^{(\alpha_{mn}+\alpha_{il}^{*})h}}{(\alpha_{mn}+\alpha_{il}^{*})}\right] \quad (68)$$

B. Lift force

The lift force from the top plate surface is calculated from

$$F_y^{top}=\frac{1}{4\mu_0}\int_0^{l}\int_0^{w}\left(B_y^{\mathrm{II}}B_y^{\mathrm{II}*}-B_x^{\mathrm{II}}B_x^{\mathrm{II}*}-B_z^{\mathrm{II}}B_z^{\mathrm{II}*}\right)\Big|_{y=0}dzdx \quad (69)$$

where

$$\begin{aligned}&\int_{x=0}^{l}\int_{z=0}^{w}B_y^{\mathrm{II}}B_y^{\mathrm{II}*}dxdz\\ &=\frac{l}{2}\sum_{m=1}^{M}\sum_{n=1}^{N_z}\sum_{l=1}^{N_z} I_{nl}^{z} q_n\alpha_{mn}\left(C_{mn}^{a}-D_{mn}^{a}\right)q_l^{*}{\alpha_{ml}}^{*}\left(C_{ml}^{a}-D_{ml}^{a}\right)^{*}\\ &-\varepsilon^{2*}\frac{l}{2}\sum_{m=1}^{M}\sum_{n=1}^{N_z}\sum_{l=1}^{N_r} I_{nl}^{z2} q_n\alpha_{mn}\left(C_{mn}^{a}-D_{mn}^{a}\right)\xi_m\left(C_{ml}^{b}+D_{ml}^{b}\right)^{*}\\ &-\varepsilon^{2}\frac{l}{2}\sum_{m=1}^{M}\sum_{n=1}^{N_r}\sum_{l=1}^{N_z} I_{nl}^{z3}\xi_m\left(C_{mn}^{b}+D_{mn}^{b}\right)q_l^{*}{\alpha_{ml}}^{*}\left(C_{ml}^{a}-D_{ml}^{a}\right)^{*}\\ &+\varepsilon^{2}\varepsilon^{2*}\frac{lw}{4}\sum_{m=1}^{M}\sum_{n=1}^{N_r}{\xi_m}^{2}\left(C_{mn}^{b}+D_{mn}^{b}\right)\left(C_{mn}^{b}+D_{mn}^{b}\right)^{*}\end{aligned} \quad (70)$$

$$\begin{aligned}&\int_{x=0}^{l}\int_{z=0}^{w}B_x^{\mathrm{II}}B_x^{\mathrm{II}*}dxdz\\ &=\frac{l}{2}\sum_{m=1}^{M}\sum_{n=1}^{N_z}\sum_{l=1}^{N_z} I_{nl}^{z}\xi_m q_n\left(C_{mn}^{a}+D_{mn}^{a}\right)\xi_m q_l^{*}\left(C_{ml}^{a}+D_{ml}^{a}\right)^{*}\\ &-\varepsilon^{2*}\frac{l}{2}\sum_{m=1}^{M}\sum_{n=1}^{N_z}\sum_{l=1}^{N_r} I_{nl}^{z2}\xi_m q_n\left(C_{mn}^{a}+D_{mn}^{a}\right)\beta_{ml}{}^{*}\left(C_{ml}^{b}-D_{ml}^{b}\right)^{*}\\ &-\varepsilon^{2}\frac{l}{2}\sum_{m=1}^{M}\sum_{n=1}^{N_r}\sum_{l=1}^{N_z} I_{nl}^{z3}\beta_{mn}\left(C_{mn}^{b}-D_{mn}^{b}\right)q_l^{*}\xi_m\left(C_{ml}^{a}+D_{ml}^{a}\right)^{*}\\ &+\varepsilon^{2}\varepsilon^{2*}\frac{lw}{4}\sum_{m=1}^{M}\sum_{n=1}^{N_r}\left|\beta_{mn}\right|^{2}\left(C_{mn}^{b}-D_{mn}^{b}\right)\left(C_{mn}^{b}-D_{mn}^{b}\right)^{*}\end{aligned} \quad (71)$$

$$\begin{aligned}&\int_{x=0}^{l}\int_{z=0}^{w}B_z^{\mathrm{II}}B_z^{\mathrm{II}*}dxdz\\ &=\frac{l}{2}\sum_{m=1}^{M}\sum_{n=1}^{N_z}\sum_{l=1}^{N_z} I_{nl}^{z5}{p_n}^{2}(C_{mn}^{a}+D_{mn}^{a})p_l^{2*}(C_{ml}^{a}+D_{ml}^{a})^{*}\end{aligned} \quad (72)$$

$$I_{nl}^{z5}=0.5\left[\frac{\sin\left[(q_n-q_l^{*})w\right]}{(q_n-q_l^{*})}+\frac{\sin\left[(q_n+q_l^{*})w\right]}{(q_n+q_l^{*})}\right] \quad (73)$$

Lift force can be computed from the bottom surface Γ_b by replacing C_{mn}^{a}, D_{mn}^{a}, C_{mn}^{b} and D_{mn}^{b} with $C_{mn}^{a}e^{-\alpha_{mn}h}$, $D_{mn}^{a}e^{\alpha_{mn}h}$, $C_{mn}^{b}e^{-\beta_{mn}h}$ and $D_{mn}^{b}e^{\beta_{mn}h}$ respectively. Lift force from the plate edge is given by

$$F_y^{side}=\frac{l}{4\mu_0}\sum_{m=1}^{M}\sum_{n=1}^{N_z}\sum_{l=1}^{N_z}\sin(q_n w)q_n\alpha_{mn}\cos(q_l^{*}w)p_l^{2*}\left[C_{mn}^{a}C_{ml}^{a}{}^{*}\frac{1-e^{-(\alpha_{mn}+{\alpha_{ml}}^{*})h}}{(\alpha_{mn}+{\alpha_{ml}}^{*})}+C_{mn}^{a}D_{ml}^{a}{}^{*}\frac{1-e^{-(\alpha_{mn}-{\alpha_{ml}}^{*})h}}{(\alpha_{mn}-{\alpha_{ml}}^{*})} + D_{mn}^{a}C_{ml}^{a}{}^{*}\frac{1-e^{(\alpha_{mn}-{\alpha_{ml}}^{*})h}}{(\alpha_{mn}-{\alpha_{ml}}^{*})}+D_{mn}^{a}D_{ml}^{a}{}^{*}\frac{1-e^{(\alpha_{mn}+{\alpha_{ml}}^{*})h}}{(\alpha_{mn}+{\alpha_{ml}}^{*})}\right] \quad (74)$$

C. Lateral force

The lateral force from the top plate surface is

$$F_z^{top}=\frac{l}{4\mu_0}\left[\sum_{m=1}^{M}\sum_{n=1}^{N_z}\sum_{l=1}^{N_z} I_{nl}^{z6}p_n^2\left(C_{mn}^a+D_{mn}^a\right)q_l^*\alpha_{ml}^*\left(C_{ml}^a-D_{ml}^a\right)^* - \varepsilon^{2*}\sum_{m=1}^{M}\sum_{n=1}^{N_z}\sum_{l=1}^{N_r} I_{nl}^{z7}p_n^2\xi_m\left(C_{mn}^a+D_{mn}^a\right)\left(C_{ml}^b+D_{ml}^b\right)^*\right] \quad (75)$$

$$I_{nl}^{z6}=0.5\left[\frac{1-\cos\left[(q_n+q_l^*)w\right]}{(q_n+q_l^*)}-\frac{1-\cos\left[(q_n-q_l^*)w\right]}{(q_n-q_l^*)}\right] \quad (76)$$

$$I_{nl}^{z7}=0.5\left[\frac{1-\cos\left[(q_n+r_l)w\right]}{(q_n+r_l)}-\frac{1-\cos\left[(q_n-r_l)w\right]}{(q_n-r_l)}\right] \quad (77)$$

Similarly lateral force from the bottom surface Γ_b can be computed. The lateral force due to side surface is

$$F_z^{side}=\frac{1}{4\mu_0}\int_0^l\int_{-h}^0 (B_z^{II}B_z^{II*}-B_x^{II}B_x^{II*}-B_y^{II}B_y^{II*})\Big|_{z=w}dydx \quad (78)$$

where

$$\int_0^l\int_{-h}^0 B_z^{II}B_z^{II*}\Big|_{z=w}dydx=\frac{l}{2}\sum_{m=1}^{M}\sum_{n=1}^{N_z}\sum_{l=1}^{N_z}\cos(q_nw)p_n^2\cos(q_l^*w)p_l^{2*}\left[C_{mn}^aC_{ml}^{a*}\frac{1-e^{-(\alpha_{mn}+\alpha_{ml}^*)h}}{\alpha_{mn}+\alpha_{ml}^*}+C_{mn}^aD_{ml}^{a*}\frac{1-e^{-(\alpha_{mn}-\alpha_{ml}^*)h}}{\alpha_{mn}-\alpha_{ml}^*} - D_{mn}^aC_{ml}^{a*}\frac{1-e^{(\alpha_{mn}-\alpha_{ml}^*)h}}{\alpha_{mn}-\alpha_{ml}^*}-D_{mn}^aD_{ml}^{a*}\frac{1-e^{(\alpha_{mn}+\alpha_{ml}^*)h}}{\alpha_{mn}+\alpha_{ml}^*}\right] \quad (79)$$

$$\int_0^l\int_{-h}^0 B_y^{II}B_y^{II*}\Big|_{z=w}dydx=\frac{l}{2}\sum_{m=1}^{M}\sum_{n=1}^{N_z}\sum_{l=1}^{N_z}\sin(q_nw)q_n\alpha_{mn}\sin(q_l^*w)q_l^*\alpha_{ml}^* \left\{C_{mn}^aC_{ml}^{a*}\frac{1-e^{-(\alpha_{mn}+\alpha_{ml}^*)h}}{\alpha_{mn}+\alpha_{ml}^*}-C_{mn}^aD_{ml}^{a}\frac{1-e^{-(\alpha_{mn}-\alpha_{ml}^*)h}}{\alpha_{mn}-\alpha_{ml}^*} +D_{mn}^aC_{ml}^{a*}\frac{1-e^{(\alpha_{mn}-\alpha_{ml}^*)h}}{\alpha_{mn}-\alpha_{ml}^*}+D_{mn}^aD_{ml}^{a*}\frac{1-e^{(\alpha_{mn}+\alpha_{ml}^*)h}}{\alpha_{mn}+\alpha_{ml}^*}\right\} \quad (80)$$

$$\int_0^l\int_{-h}^0 B_x^{II}B_x^{II*}\Big|_{z=w}dydx=\frac{l}{2}\sum_{m=1}^{M}\sum_{n=1}^{N_z}\xi_m^2\sin(q_nz)q_n\sin(q_l^*z)q_l^* \left[C_{mn}^aC_{ml}^{a*}\frac{1-e^{-(\alpha_{mn}+\alpha_{ml}^*)h}}{\alpha_{mn}+\alpha_{ml}^*}+C_{mn}^aD_{ml}^{a*}\frac{1-e^{-(\alpha_{mn}-\alpha_{ml}^*)h}}{\alpha_{mn}-\alpha_{ml}^*} - D_{mn}^aC_{ml}^{a*}\frac{1-e^{(\alpha_{mn}-\alpha_{ml}^*)h}}{\alpha_{mn}-\alpha_{ml}^*}-D_{mn}^aD_{ml}^{a*}\frac{1-e^{(\alpha_{mn}+\alpha_{ml}^*)h}}{\alpha_{mn}+\alpha_{ml}^*}\right] \quad (81)$$

VIII. Acknowledgment

The authors would gratefully like to thank the JMAG Corporation for the use of their FEA software.

IX. References

[1] I. Boldea, A. Trica, G. Papusoiu, and S. A. Nasar, "Field tests on a MAGLEV with passive guideway linear inductor motor transportation system," *IEEE Transactions on Vehicular Technology,* vol. 37, pp. 213-219, 1988.

[2] J. A. Ross, "ROMAG transportation system," *Proceedings of the IEEE,* vol. 61, pp. 617-620, 1973.

[3] J. F. Eastham and E. R. Laithwaite, "Linear induction motors as `electromagnetic rivers'," *Electrical Engineers, Proceedings of the Institution of,* vol. 121, pp. 1099-1108, 1974.

[4] N. Fujii, M. Chida, and K. Ogawa, "Three dimensional force of magnet wheel with revolving permanent magnets," *IEEE Transactions on Magnetics,* vol. 33, pp. 4221-4223, 1997.

[5] N. Fujii, G. Hayashi, and Y. Sakamoto, "Characteristics of magnetic lift, propulsion and guidance by using magnet wheels with rotating permanent magnets," in *Conference Record of the 2000 IEEE Industry Applications Conference, 2000.* , 2000, pp. 257-262 vol.1.

[6] J. Bird, "An investigation into the use of electrodynamic wheels for high speed ground transportation," Ph.D, Electrical Engineering, University of Wisconson - Madison, Madison, 2007.

[7] L. Urankar, "Electrodynamics of finite fidth guideway Maglev systems in an integral equation formulation," *Siemens Forschung Entwicklungsberichte,* vol. 8, pp. 204-208, 1979.

[8] A. Skarlatos and T. Theodoulidis, "Solution to the eddy-current induction problem in a conducting half-space with a vertical cylindrical borehole," *Proceedings of the Royal Society A,* vol. 468, pp. 1758-1777, 2012.

[9] T. P. Theodoulidis and J. R. Bowler, "Eddy current coil interaction with a right-angled conductive wedge," *Proceedings of the Royal Society A: Mathematical, Physical and Engineering Science,* vol. 461, pp. 3123-3139, October 8, 2005 2005.

[10] T. Theodoulidis and J. R. Bowler, "Eddy-current interaction of a long coil with a slot in a conductive plate," *IEEE Transactions on Magnetics,* vol. 41, pp. 1238-1247, 2005.

[11] T. Theodoulidis and J. R. Bowler, "Interaction of an eddy-current coil with a right-angled conductive wedge," *IEEE Transactions on Magnetics,* vol. 46, pp. 1034-1042, 2010.

[12] K. J. W. Pluk, B. L. J. Gysen, J. L. G. Janssen, E. A. Lomonova, and J. W. Jansen, "Modeling of a finite, rectangular, conducting plate in an eddy current damper," in *XXth International Conference on Electrical Machines (ICEM), 2012*, 2012, pp. 2846-2851.

[13] C. M. Hebbert, "Some Applications of the Method of Images—II," *Physical Review,* vol. 17, pp. 157-160, 1921.

[14] S. Paul and J. Bird, "A 3-D analytic eddy current model for a finite width conductive plate," *COMPEL: The International Journal for Computation and Mathematics in Electrical and Electronic Engineering,* vol. 33, pp. 688–706, 2014.

[15] S. Paul and J. Z. Bird, "Analytic 3-D eddy current model of a finite width conductive plate including edge-effects," *International Journal of Applied Electromagnetics and Mechanics* vol. 45, pp. 565-571, 2014.

[16] S. Paul, "Three-dimensional steady state and transient eddy current modeling," PhD, Electrical and Computer Engineering, University of North Carolina at Charlotte, Charlotte, 2014.

[17] W. R. Smythe, *Static and Dynamic Electricity*, Second ed.: McGraw-Hill Book Company Inc., 1950.

[18] S. Paul, D. Bobba, N. Paudel, and J. Z. Bird, "Source field modeling in air using magnetic charge sheets," *IEEE Transactions on Magnetics,* vol. 48, pp. 3879-3882, 2012.

[19] Z. P. Xia, Z. Q. Zhu, and D. Howe, "Analytical magnetic field analysis of Halbach magnetized permanent-magnet machines," *IEEE Transactions on Magnetics,* vol. 40, pp. 1864-1872, 2004.

X. Biographies

S. Paul received his B.E (1st Class Hons.) in Instrumentation and Electronics Engineering from Jadavpur University, India in 2006 and PhD degree in Electrical Engineering from the University of North Carolina-Charlotte, USA in 2014. He is now with Nexteer Automotive, Saginaw, MI. His research interests include low frequency electromagnetics, electric machines and sensor design.

J.Z. Bird obtained his B.E. (1st Class Hons.) from the University of Auckland, New Zealand, in 2000 and his M.S. and Ph.D. from the University of Wisconsin-Madison, USA in 2004 and 2006 respectively. From January 2007 to December 2008 he was a senior design engineer at General Motor's Advanced Technology Center in Torrance, CA. From 2009 to 2015 he was an Assistant Professor at the University of North Carolina at Charlotte (UNCC). Currently he is an Associate Professor at the Department of Electrical and Computer Engineering of Portland State University. Professor Bird's research areas are at the intersection of applied electromagnetics, mechanics and controls.